1. Tomasz RYMARCZYK[1,2], 2. Grzegorz KŁOSOWSKI[3], 3. Konrad NIDERLA[1,2]

WSEI University (1), Research and Development Center Netrix S.A. (2), Lublin University of Technology (3)
ORCID: 1. 0000-0002-3524-9151; 2. 0000-0001-7927-3674. 3. 0000-0003-1280-0622

doi:10.15199/48.2023.06.29

Advantages of convolutional neural network compared to multilayer perceptron in electrical tomography

Abstract. *This article deals with the optimization of the artificial neural network (ANN) architecture in order to improve the quality of tomographic imaging. During the research, many variants of predictive models were tested, differing in the number of neurons, the number and type of layers, learning algorithm, transfer functions, overfitting prevention methods, etc. As a result of comparing the results in the form of reconstruction images obtained with reference images, the optimal architecture of the neural network was selected. Noteworthy is the original approach of training separate ANNs for each image voxel separately. As a result, the model consists of many independently trained, single-output ANNs that form a structure referred to as a multiple neural network (MNN).*

Streszczenie. *Niniejszy artykuł dotyczy problematyki optymalizacji architektury sztucznej sieci neuronowej (SSN) w celu podniesienia jakości obrazowania tomograficznego. W trakcie badań testowano wiele wariantów modeli predykcyjnych, różniących się liczbą neuronów, liczbą i rodzajem warstw, algorytmem uczenia, funkcjami transferowymi, metodami zapobiegania przeuczeniu itp. W wyniku porównania rezultatów w postaci uzyskanych obrazów rekonstrukcyjnych z obrazami referencyjnymi wybrano optymalną architekturę sieci neuronowej. Na uwagę zasługuje oryginalne podejście polegające na trenowaniu osobnych ANN dla każdego woksela obrazu z osobna. W rezultacie model składa się z wielu niezależnie trenowanych, jednowyjściowych SSN, które tworzą strukturę określoną jako wielokrotna sieć neuronowa (WSN). (**Zalety konwolucyjnej sieci neuronowej w porównaniu z perceptronem wielowarstwowym w tomografii elektrycznej**)*

Keywords: electrical tomography; machine learning; industrial tomography.
Słowa kluczowe: tomografia elektryczna; uczenie maszynowe; tomografia przemysłowa.

Introduction

Electrical process tomography, which permits non-invasive diagnosis of the interior of numerous industrial devices, is a field that is actively evolving [1]. Tomography in particular makes it feasible to observe flat and spatial cross-sections of structures like pipes, tanks, and chemical reactors effectively [1–3]. The parameters of the industrial process should be continuously examined in order to ensure appropriate operation [4]. Such a metric might be the degree of crystallization in the context of industrial reactors [5]. This is relevant to liquid-filled tank reactors because crystals may precipitate or create gas bubbles as a result of the changes occurring [6]. The degree of liquid crystallization, which is measured by the quantity and size of crystals, and the degree of liquid gassing, which is determined by the quantity and distribution of gas bubbles, both attest to the effectiveness of the procedure [7]. Hence, by altering the mixing speed, temperature, pressure, substrate chemical composition, or flow intensity, for example, while knowing the process's current state, you can affect its characteristics. Liquid, solid, and gas phases of a substance going through physical and chemical changes can all be present in an industrial chemical reactor. Crystals, solid particles, or gas bubbles may develop in the liquid under specific circumstances [8].

Materials and methods

In order to tackle the inverse problem in industrial electrical impedance tomography (EIT), the study examined the best ways to apply artificial neural networks (ANN) and/or convolutional neural networks (CNN) [9–11]. In the initial model under consideration, several neural networks (MANN) were included. Each MANN had measurements as its input and an output that was a real number that represented the value of a particular voxel [12]. The second model takes into account training CNN using the input data vector (1D). 32 electrodes are positioned all around the tested reactor for the tomograph. For each test case, there were 448 voltage readings taken between the various electrode pairs. The resolution of the 3D picture was 14100, hence there are 14,100 individually trained ANNs with a single output in the MANN structure. $\mathbf{MNN} = (\mathbf{448} \to \mathbf{20} \to \mathbf{1}) \times \mathbf{14100}$ can be used to specify an MNN's structure. All of the networks included in the MANN, according to the aforementioned model, have 20 neurons in the hidden layer. Figure 1 depicts the MANN flow diagram. As you can see, the trick is to give each voxel of the output image its own neural network. The neural network that directly creates the value of each of the 14100 voxels has less computational complexity as a result of this novel technique. The general operating principle of CNN is depicted in Figure 2 [13].

In one pass, a homogeneous neural network converts 448 inputs into 14,100 outputs. There were 30,000 examples in the collection of all observations. Table 1 shows the outcomes of training the multilayer perceptron network for a randomly chosen voxel. MSE was the primary metric used to rate the MANN neural network's performance during training. The mean squared error (MSE), which is satisfied by the formula, is the difference between patterns and reconstruction images (1)

$$\text{MSE} = \frac{\sum_{i=1}^{n}(y_i - \hat{y}_i)^2}{n} \tag{1}$$

where n — is the sum of the number of finite elements in the image mesh and the number of voxels in the picture, y_i — the reference value of *i*-th pixel, $\hat{y}_i$ — the value of reconstruction of *i*-th pixel. R stands for regression R-value. It shows how patterns and reconstructions are related. In the ratios of 70:30:30, the collection of observations was split into three subsets: training, validation, and test.

Table 1. Parametric ANN learning results for a selected voxel

Sets	Observations	MSE	R
Training	21000	0.0011	0.9361
Validation	4500	0.0018	0.8914
Test	4500	0.0011	0.9304

The test stand used to validate the tomographic measurements is depicted in Figure 3. A series of electrodes for EIT measurements surrounds the reservoir on the left side. On the right, a tomograph can be shown

that uses carefully chosen current parameters, including voltage and amperage, to deliver electric current to the appropriate pairs of electrodes in a predetermined order.

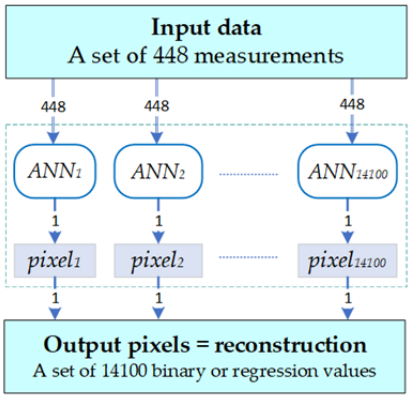

Fig. 1. Workflow of multiple artificial neural network (MANN)

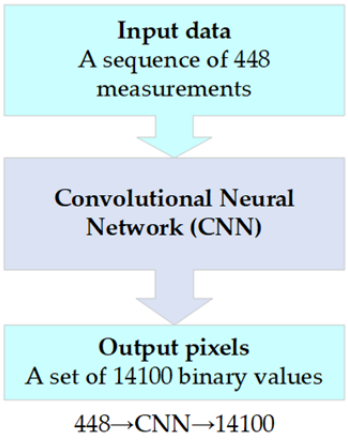

Fig. 2. Workflow of a convolutional neural network (CNN)

Fig. 3. The test stand: on the left side is the reactor model with electrodes, and on the right side there is a tomograph

The sequential (1D) first layer of CNN has 448 measurement values. A convolutional layer with seven 160-element filters makes up the second layer. The ReLu layer, which is the following layer, is intended to zero out negative numbers. The global max pooling layer is the fourth layer. In this network, the layer pools throughout the spatial dimension are used to achieve downsampling by generating an output that is maximal in all of the spatial dimensions of the input. Fully linked layers apply bias to each input as well as the total of the input and weight products. There are 5000 neurons in the fifth layer and 14100 neurons in the sixth layer. The MSE is calculated after each iteration in the regression input layer.

The CNN learning process can be seen in Figure 4. The root mean square error is the quality assessment criterion (RMSE). The fact that all three lines displaying the training validation and test set faults are highly concurrent shows that the training procedure was done correctly. At epoch 12, the best validation performance of 0.0017883 was attained. The hyperbolical trajectory of the error line during CNN and MANN training demonstrates the absence of overfitting and raises expectations for a highly effective prediction model.

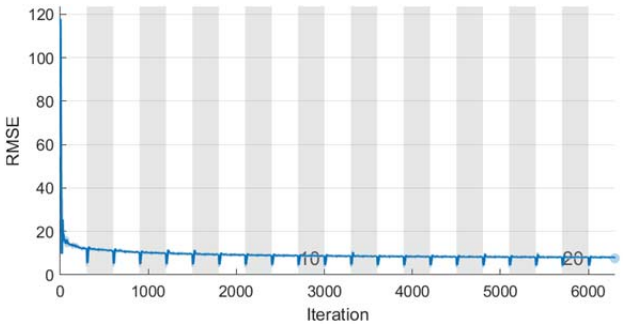

Fig. 4. CNN training performance (RMSE) for a randomly selected voxel

Figure 5 shows a graph of the learning process using MSE as a quality criterion.

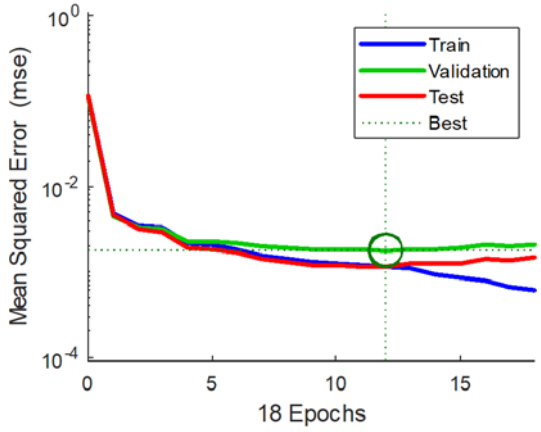

Fig. 5. ANN training performance (MSE) for a randomly selected voxel

The early halting strategy was employed to guard the neural network against overfitting. The approach relies on using a validation set to automatically finish the training phase. If the learning error does not reduce during the following six rounds, the training process is terminated. The requirement to put up a relatively tiny minibatch leads to minor, cyclical changes in the CNN training performance chart. The GPU being used has memory restrictions, which contribute to this.

Results

A comparison of the MANN and CNN reconstruction techniques is shown in Figure 6. Reference pictures can be found in the first column. The MANN model-generated reconstructions are displayed in the second column, while the CNN-produced tomographic pictures are displayed in the third column.

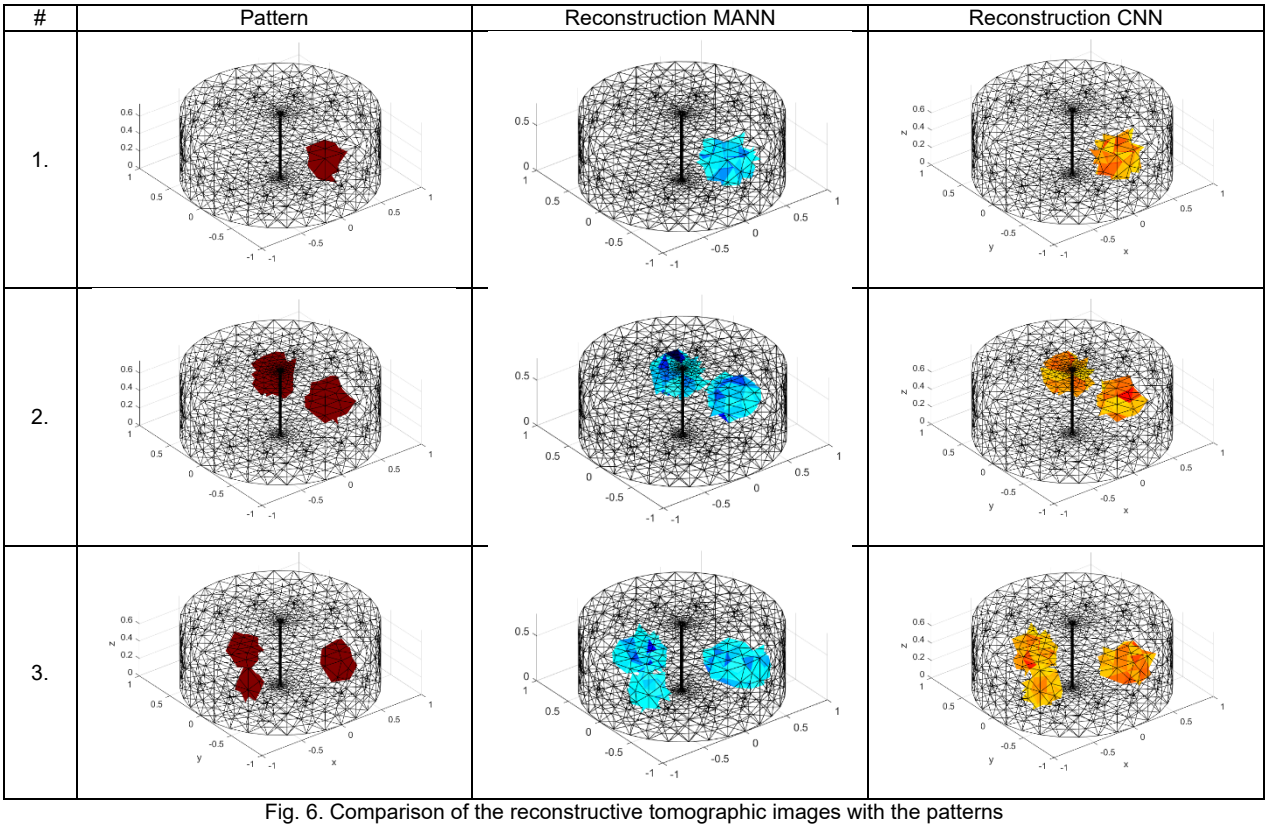

Fig. 6. Comparison of the reconstructive tomographic images with the patterns

Three cases are included in the comparison, each with unique inclusion counts, shapes, sizes, and locations. The non-obvious disparities between the MANN and CNN reconstructions are what stand out right away. A closer look at the photos reveals that the MANN approach produces inclusions that are larger than those produced by CNN. Since patterns are produced by CNN, it may be assumed that CNN is more accurate than MANN.

It was determined to employ four indicators: mean square error (MSE), normalized mean square error (NMSE), relative image error (RIE), and image correlation coefficient to provide an objective comparison assessment (ICC) [14]. In the section before, equation (1) provided a description of the MSE metric. The Euclidean norm of MSE is known as normalized mean squared error (NMSE), and it is calculated as $\mathrm{NMSE} = \|\mathrm{MSE}\|$. The RIE indicator is described in formula (2).

$$\mathrm{RIE} = \frac{\|\hat{y}-y\|}{\|y\|} \tag{2}$$

Since the MSE, NMSE, and RIE indicators measure errors, the better the model being evaluated, the lower their values. The ICC is the final indicator used. Since it measures correlation, the more closely the value approaches 1, the better for the model. The formula for the ICC computation is provided (3)

$$\mathrm{ICC} = \frac{\sum_{i=1}^{N}(y_i-\bar{y})(\hat{y}_i-\bar{\hat{y}})}{\sqrt{\sum_{i=1}^{N}(y_i-\bar{y})^2\sum_{i=1}^{N}(\hat{y}_i-\bar{\hat{y}})^2}} \tag{3}$$

where: $\bar{\hat{y}}$ is the mean voxel values of the reconstructed image and $\bar{y}$ is the mean ground-truth voxel values of the reference image.

Based on the four aforementioned variables, Table 2 provides a quantitative comparison of the two approaches (MANN and CNN). Because Table 2 evaluates the same three observations as Figure 6, it relates to Figure 6. There is only one inclusion in observation #1.

All three categories of errors, MSE, NMSE, and RIE, are bigger for MANN than for CNN. The ICC for CNN, on the other hand, is up to 10% greater than the ICC determined using the MANN approach. The other two observations have the same truth. None of the four indications supported the MANN technique in any of the examined scenarios. The average outcomes of the ratio analysis are shown in the final column of Table 2. Once more, it came out that every indicator favors CNN. In other words, the quantitative analysis done using indicators demonstrated a definite and unequivocal dominance of the CNN approach over MANN.

Table 2. Comparison of the values of qualitative indicators for both compared models – MANN and CNN

Method	Indicator	Observation #1	Observation #2	Observation #3	Average
MANN	MSE	0.00173	0.00479	0.00613	0.00422
	NMSE	0.00478	0.00388	0.00581	0.00482
	RIE	0.70622	0.61952	0.75966	0.69514
	ICC	0.70886	0.78215	0.66800	0.71967
CNN	MSE	0.00124	0.00358	0.00475	0.00319
	NMSE	0.00343	0.00290	0.00450	0.00361
	RIE	0.59876	0.53559	0.66849	0.60095
	ICC	0.80100	0.84868	0.74919	0.79963

Conclusions

Industrial tomography is a field that offers remedies that support technological advancement [15]. High accuracy and dynamics are frequently found in contemporary industrial processes. In essence, they are two opposing objectives that, nonetheless, must be accomplished if the business is to remain competitive. A good product may be produced quickly and supplied to the market with the help of accuracy and speed in the field of industrial process control. Industrial process automation is the only way to accomplish both objectives at once. Automation, on the other hand, necessitates ongoing supervision using the proper

measuring sensors and software that can evaluate the measurements and make inferences about the necessary remedial measures. The only approach that has been found to yet that allows for inside imaging of an item without endangering its structure or interfering with its internal operations is tomography [9,16].

The purpose of this study was to evaluate the MANN and CNN methodologies' applicability in industrial electrical tomography. For this objective, two models were trained, with the help of which a number of reconstructions were constructed. The four indicators MSE, NMSE, RIE, and ICC as well as a subjective comparison of the reconstructions were used. The conclusions are that both approaches provide reasonably accurate reconstructions, making them both viable for resolving the tomographic inverse problem. A more thorough investigation, particularly the index ones, shows that the CNN method is superior to MANN.

***Authors**: Tomasz Rymarczyk, Prof. Eng., WSEI University, Projektowa 4, Lublin, Poland, E-mail: tomasz.rymarczyk@netrix.com.pl; Grzegorz Kłosowski, Ph.D. Eng., Lublin University of Technology, Nadbystrzycka 38A, Lublin, Poland, E-mail: g.klosowski@pollub.pl; Konrad Niderla, M.Sc. Eng., Lublin University of Economics and Innovation, Projektowa 4, Lublin, Poland, E-mail: konrad.niderla@wsei.lublin.pl.*

REFERENCES

[1] Kłosowski G, Rymarczyk T, Cieplak T, Niderla K, Skowron Ł. Quality assessment of the neural algorithms on the example of EIT-UST hybrid tomography. Sensors (Switzerland) 2020;20. https://doi.org/10.3390/s20113324.

[2] Rymarczyk T, Kłosowski G. Innovative methods of neural reconstruction for tomographic images in maintenance of tank industrial reactors. Eksploatacja i Niezawodnosc -- Maintenance and Reliability 2019;21:261–7.

[3] Nordin N, Idroas M, Zakaria Z, Ibrahim MN. Tomographic image reconstruction of monitoring flaws on gas pipeline based on reverse ultrasonic tomography. 2014 5th International Conference on Intelligent and Advanced Systems (ICIAS), IEEE; 2014, p. 1–6. https://doi.org/10.1109/ICIAS.2014.6869445.

[4] Soleimani M. Super-sensing through industrial process tomography. Philosophical Transactions: Mathematical, Physical and Engineering Sciences 2016;374:1–5.

[5] Kłosowski G, Rymarczyk T, Kania K, Świć A, Cieplak T. Maintenance of industrial reactors supported by deep learning driven ultrasound tomography. Eksploatacja i Niezawodnosc - Maintenance and Reliability 2020;22:138–47. https://doi.org/10.17531/ein.2020.1.16.

[6] Xin LP, Yu B, Yu J. A novel control for a continuous stirred tank reactor. Chinese Control Conference, CCC, vol. 2021-July, 2021. https://doi.org/10.23919/CCC52363.2021.9549663.

[7] Wang M. Industrial tomography: systems and applications. Woodhead Publishing; 2015. https://doi.org/https://doi.org/10.1016/C2013-0-16466-5.

[8] Tian G, Yang B, Dong M, Zhu R, Yin F, Zhao X, et al. The effect of temperature on the microbial communities of peak biogas production in batch biogas reactors. Renew Energy 2018;123:15–25. https://doi.org/10.1016/J.RENENE.2018.01.119.

[9] Kozlowski E, Rymarczyk T, Cieplak T, Klosowski G, Tchorzewski P. Application of logistic regression to image reconstruction in EIT. 2019 International Interdisciplinary PhD Workshop (IIPhDW 2019), 2019, p. 80–3. https://doi.org/10.1109/IIPHDW.2019.8755407.

[10] Korzeniewska E, Sekulska-Nalewajko J, Gocławski J, Dróżdż T, Kiełbasa P. Analysis of changes in fruit tissue after the pulsed electric field treatment using optical coherence tomography. The European Physical Journal Applied Physics 2020;91:30902. https://doi.org/10.1051/EPJAP/2020200021.

[11] Rymarczyk T, Kozłowski E, Kłosowski G. Electrical impedance tomography in 3D flood embankments testing – elastic net approach. Transactions of the Institute of Measurement and Control 2019;42:680–90. https://doi.org/10.1177/0142331219857374.

[12] Rymarczyk T, Kłosowski G, Hoła A, Sikora J, Wołowiec T, Tchórzewski P, et al. Comparison of Machine Learning Methods in Electrical Tomography for Detecting Moisture in Building Walls. Energies (Basel) 2021;14:2777. https://doi.org/10.3390/en14102777.

[13] Yuen B, Dong X, Lu T. Inter-Patient CNN-LSTM for QRS Complex Detection in Noisy ECG Signals. IEEE Access 2019;7:169359–70. https://doi.org/10.1109/ACCESS.2019.2955738.

[14] Kłosowski G, Rymarczyk T, Niderla K, Rzemieniak M, Dmowski A, Maj M. Comparison of machine learning methods for image reconstruction using the LSTM classifier in industrial electrical tomography. Energies (Basel) 2021;14. https://doi.org/10.3390/en14217269.

[15] Wajman R, Banasiak R, Babout L. On the Use of a Rotatable ECT Sensor to Investigate Dense Phase Flow: A Feasibility Study. Sensors 2020, Vol 20, Page 4854 2020;20:4854. https://doi.org/10.3390/S20174854.

[16] Fabijańska A, Banasiak R. Graph convolutional networks for enhanced resolution 3D Electrical Capacitance Tomography image reconstruction. Appl Soft Comput 2021;110:107608. https://doi.org/10.1016/J.ASOC.2021.107608.